Int. J. Electrochem. Sci., 15 **(2020)** 6841 – 6851, doi: 10.20964/2020.07.57

International Journal of
ELECTROCHEMICAL
SCIENCE
www.electrochemsci.org

Hydrangea-like Mesoporous Carbon Architectures Embedded with MnO_x Nanoparticles for Solid-State Asymmetric Supercapacitors with Enhanced Areal Capacitance

Yan Feng[1], *Henghan Dai*[1], *Li Liu*[1], *Aoning Wang*[1], *Yingjie Zhou*[2,*], *Gengzhi Sun*[1,*] *and Xiang Liu*[1,*]

[1] Institute of Advanced Materials (IAM), Nanjing Tech University (Nanjing Tech), Nanjing 211816, China
[2] State Key Laboratory for Modification of Chemical Fibers and Polymer Materials, College of Materials Science and Engineering, Donghua University, Shanghai, 201620, China
[*]E-mail: zhouyj@dhu.edu.cn ; iamgzsun@njtech.edu.cn ; iamxliu@njtech.edu.cn

Received: 4 March 2020 / *Accepted:* 21 April 2020 / *Published:* 10 June 2020

Hydrangea-like mesoporous carbon architectures embedded with MnO_x nanoparticles (MnO_x@C) are synthesized *via* the pyrolysis of Mn-MOFs (Mn-based metal organic frameworks) grwon on nickel foam as a binder-free electrode for asymmetric supercapacitors. The as-prepared MnO_x@C featuring stacked carbon flakes with mesoporous structure and embedded with nanosized MnO_x particles exhibit superior electrochemical performances with a specific areal capacitance of 1518 mF cm^{-2} at a current density of 3 mA cm^{-2}. An asymmetric supercapacitor that is fabricated using MnO_x@C as cathode and activated carbon as anode demonstrates remarkable areal power density of 12.2 W cm^{-2}, areal energy density of 169.4 mWh cm^{-2} and excellent rate capability. This work provides a facile and effective strategy to construct MnO_x@C supercapacitive materials so as to efficiently enhance electron transport at the meantime achieve rapid ion diffusion.

Keywords: metal organic frameworks, mesoporous carbon, manganese oxide, binder-free electrodes, asymmetric supercapacitors

1. INTRODUCTION

Supercapacitors have gained worldwide attention in recent years due to their ultra-long lifespan, high power density and fast charge/discharge rate in comparison with rechargeable batteries[1, 2]. However, the major challenge in this research area remains to obtain high performance supercapacitors with improved energy density without compromising power density. According to equation of $E = ½CV^2$, where E, C and V represent energy density, capacitance and working voltage of the supercapacitors, the well adopted strategy is to develop high capacitance electrode materials at the meantime use asymmetric device design to extend the operating voltages[3-8]. To date, numerous redox

materials have been applied as electrode for supercapacitors, including MnO_x[9-13], CoO_x[14], FeO_x[15-17], NiO[18-21] and *etc.*, among which MnO_x is considered as the most promising electrode material owing to its large theoretical specific capacitance, low cost and non-toxic environmental compatibility[22]. Nevertheless, the practical application of MnO_x in energy storage is severely hindered by its low intrinsic conductivity. Hybridizing nanosized MnO_x with carbonaceous materials has been demonstrated as a promising method to solve this problem[23-25]. Therefore, it is highly desired to develop a facile and effective strategy to embed MnO_x nanoparticles in porous carbon matrix so as to efficiently enhance electron transport at the meantime achieve rapid ion diffusion.

Metal-organic frameworks (MOFs) are widely known for their tunable and porous architectures, which enables their potential applications in catalysis, gas storage, drug delivery, supercapacitors, Li-ion batteries and so on[26-30]. Recent pioneer works have demonstrated that a number of electrochemically active materials ranging from metal oxides/sulphides, hierarchically porous carbon, and their hybrids can be derived from their parent MOF-precursors offering improved energy storage capability due to the stable physicochemical properties, high surface specific area and controlled porosity[31-34].

In this work, hydrangea-like mesoporous carbon architectures uniformly embedded with MnO_x nanoparticles (termed as MnO_x@C) were prepared through the pyrolysis of Mn-based MOFs which were grown on nickel foam *via* hydrothermal reaction. The obtained composites having distinct topological morphology from that of Mn-MOFs and a high specific surface area exhibited a high areal capacitance of 1518 mF cm^{-2} with outstanding rate capability that the capacitance retention is about 65% when discharge current increases from 3 to 12 mA cm^{-2}. The asymmetric supercapacitors (ASCs) based on such MnO_x@C hybrid delivered an improved areal energy density of 169.4 mWh cm^{-2} at the power density of 12.2 W cm^{-2}.

2. EXPERIMENTAL SECTION

Nickle foam (NF, porosity ≥ 98%), manganese nitrate tetrahydrate ($Mn(NO_3)_2·4H_2O$, 99.5%), pure terephthalic acid (PTA, $C_6H_4(COOH)_2$, 99.5%), N,N-dimethylformamide (C_3H_7NO, 99.5%), polyvinyl alcohol (PVA, 99.0%), sodium sulfate decahydrate ($Na_2SO_4·10H_2O$, 99.5%) were purchased from Aladdin and used directly.

Typically, a piece of NF (1×3 cm) was immersed in 2 M HCl under ultrasonication for 10 min to remove surface NiO and any contaminations. After being rinsed with deionized water and ethanol several times, it was dried at 60 ºC for 8 h. Then, 16 mmol $Mn(NO_3)_2·4H_2O$ and 8 mmol PTA dissolved in 60 mL DMF together with the pretreated NF were transferred to a Teflon-lined stainless steel autoclave. The autoclave was sealed and maintained at 160 ºC for 24 h. After cooling down to room temperature, the NF loaded with Mn-MOF precursor was cleaned by ethanol three times to get rid of the unreacted reagents and then dried at 60 ºC for 12 h. Finally, the Mn-MOF was annealed under Ar at 900 ºC for 2 h to obtain MnO_x@C.

The asymmetric supercapacitor was assembled by using MnO_x@C as cathode and activated carbon (AC) as anode, and PVA-Na_2SO_4 gel as electrolyte, respectively, in face-to-face manner. The PVA-Na_2SO_4 gel electrolyte was prepared by mixing 6 g PVA and 6 g $Na_2SO_4 \cdot 10H_2O$ in 60 mL deionized water by stirring at 85 ºC for 2 h, followed by cooling down to room temperature. The fabrication of asymmetric device (MnO_x@C//AC) is presented in Fig. 1.

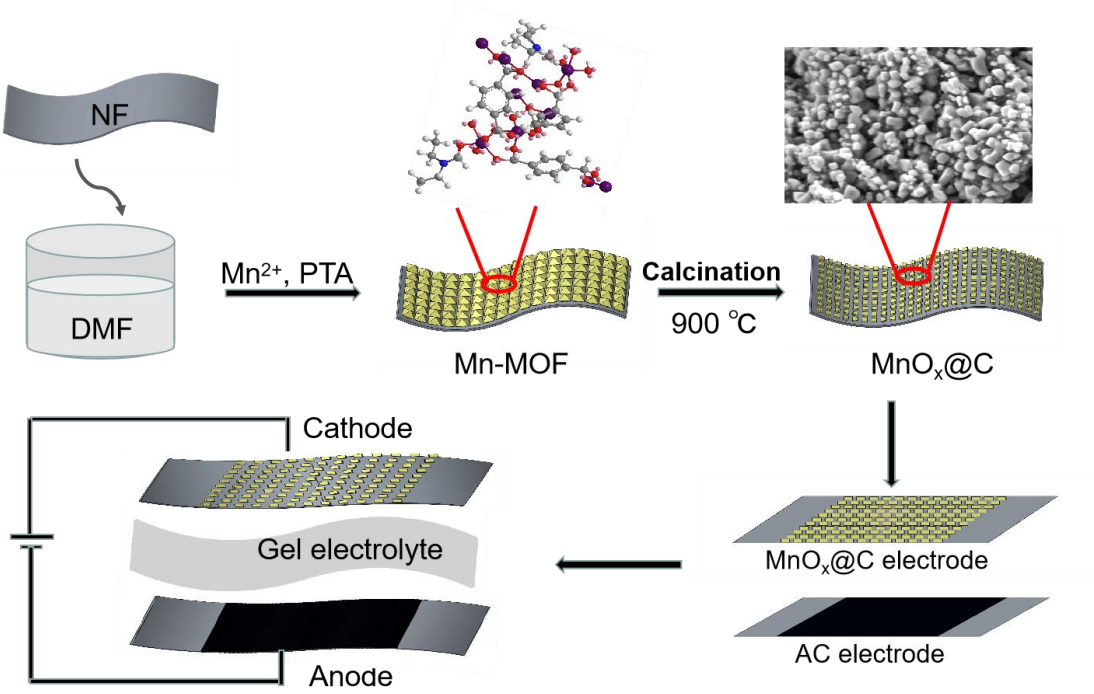

Figure 1. Schematic illustration of synthesizing MnO_x@C and the construction of ASC device.

X-ray diffraction (XRD) patterns were collected using a Rigaku Smartlab diffractometer equipped with a Cu Kα (λ = 0.154059 nm) radiation source between 3° and 80°. Scanning electron microscopy (SEM) images were observed on JEOL JSM-7800F scanning electron microscope equipped with an Energy Dispersive Spectrometer (EDS). High-resolution transmission electron microscopy (TEM) were performed on JEOL JEM-2010F. The Brunner-Emmett-Teller (BET) surface area and the pore-size distribution were measured by nitrogen adsorption/desorption on a BELSORP-mini instrument. X-ray photoelectron spectroscopy (XPS) analysis was demonstrated using an EscaLab 250Xi instrument, and the spectra were alignment using C 1s peak.

The electrochemical performances of individual electrode were investigated in a three-electrode system with a CHI 660E electrochemical work-station using 0.5 M Na_2SO_4 as electrolyte. The MnO_x@C, Ag/AgCl electrode, and Pt wire were used as the working electrode, reference electrode, and counter electrode, respectively. Cyclic voltammetry (CV) tests were conducted in the potential range of 0.0-1.0 V (*vs*. Ag/AgCl electrode) at the scanning rates of 5, 10, 25, 50, 75, and 100 mV s^{-1}, respectively. The galvanostatic charge/discharge (GCD) measurements were carried out between 0.0 and 1.0 V at the current densities of 3, 5, 7, 9, and 12 mA cm^{-2}, respectively. The electrochemical impedance spectroscopy (EIS) also tested by the CHI 660E. The area specific capacitance of the single electrode

and the areal energy density as well as areal power density of asymmetric device were calculated from the discharge curve based on the following equations:

$$C_A = \frac{t\int \mathrm{i} \times du}{A \times \Delta u} \quad (1)$$

$$C_A = \frac{i \times t}{A\Delta u} \quad (2)$$

$$E_A = \frac{\mathrm{C_A} \times (\Delta u)^2}{2 \times 3600} \quad (3)$$

$$P_A = \frac{\mathrm{E_A} \times 3600}{\mathrm{t}} \quad (4)$$

where C is the specific areal capacitance, i is the discharging current density, Δu is the potential (V), A is the geometrical area of electrode (cm^2), and t is the discharging time[35, 36]. The electrochemical performances of the asymmetric devices were tested in a two-electrode configuration.

3. RESULTS AND DISCUSSION

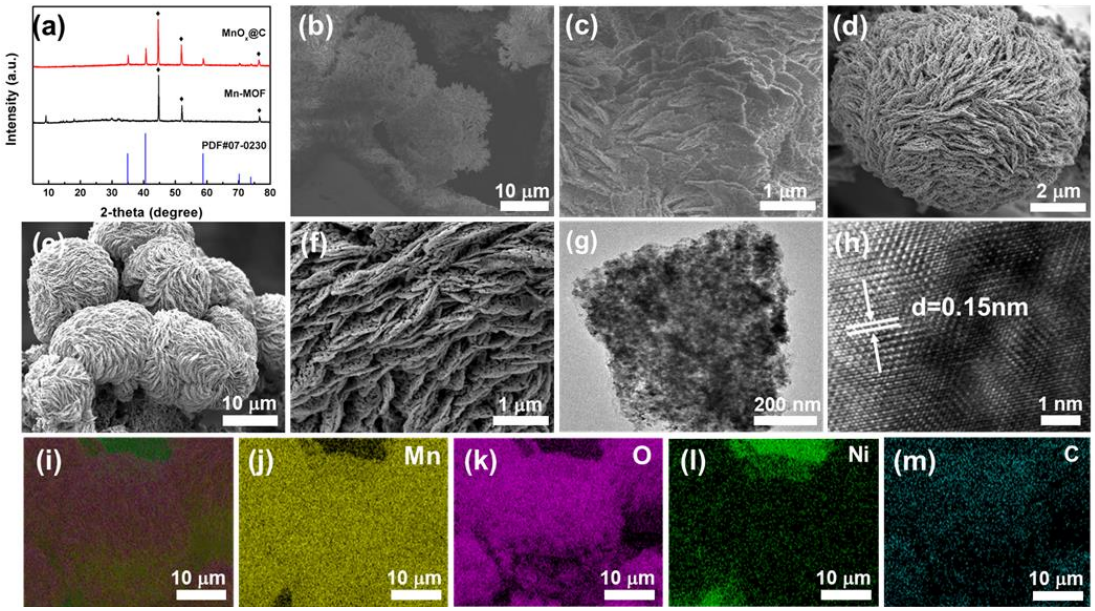

Figure 2. (a) XRD pattern of MnO_X@C and Mn-MOF, (b,c) SEM images of the structure of Mn-MOF, (d-f) SEM, (g) TEM and (h) HRTEM images of MnO_x@C, (i-m) EDS elemental mappings of Mn, O, Ni, C.

As shown in Fig. 2a, XRD pattern of MnO_x@C matches well with MnO (JCPDF file no. 07-0230 with the standard peaks indicated by the red lines)[37], suggesting the complete conversion from Mn-MOFs to MnO during pyrolysis. Fig. 2b and 2c present the pristine Mn-MOFs before calcination, which are assembled into hierarchical architectures. Interestingly, after calcination, hydrangea-like structure was obtained as shown in Fig. 2d and 2e. Mesoporous carbon architectures are embedded with plenty of MnO_x nanoparticles (Fig. 2f) that are evenly distributed with boundaries clearly identified (Fig.

2g). High resolution TEM (HRTEM) image shows a lattice spacing of 0.15 nm (Fig. 2h) which corresponds to the theoretical interplane spacing of MnO (220), confirming the formaiotn of highly crystalline MnO particles. This result is in good accordance with that observed in XRD. The element-mapping of MnO_x@C (Fig. 2i-2m) gives evidence on the uniform distribution of Mn, C, and O in MnO_x@C nanocomposites[38], and Ni belongs to NF substrate. According to the EDS results, as seen in Table 1, the atomic ratio of Mn to O is 1.13:1.50, suggesting that other than Mn^{2+} higher Mn valence might exist in the nanocomposites[39].

Table 1. The content of each element of the MnO_x@C in the EDS test.

Element	C	O	Si	Mn	Ni
Weight percentage (wt%)	4.44	24.05	0.11	61.86	9.54

TEM image presented in Fig. 3a clearly shows that the average particle size of MnO_x is around 20 nm. Hydrangea-like MnO_x@C has mesoporous strucutres with a specific surface area of 241.46 $m^2 g^{-1}$ and an average pore size of 5.96 nm (Fig. 3b), which are much larger than those reported[40]. Such a unique strucutre is highly desired for the advantages of fast ion and electron transportation during electrochemical charge-discharge process.

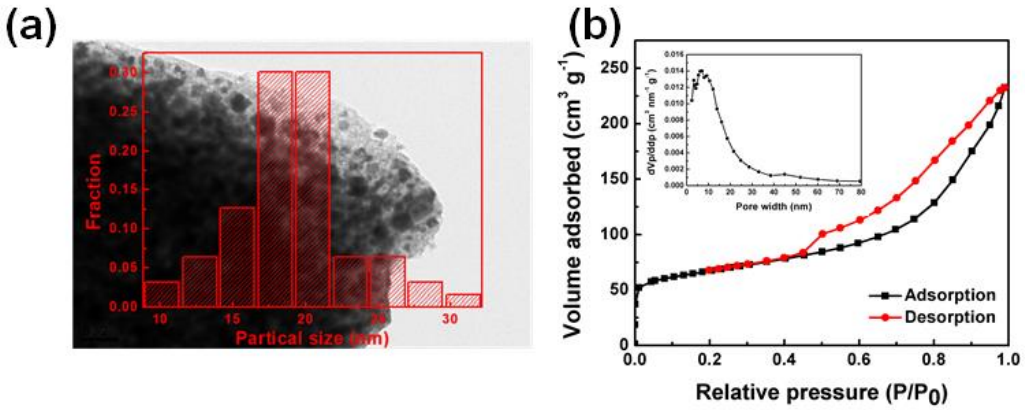

Figure 3. (a) Particle size distribution of MnO_x@C, (b) N_2 adsorption-desorption isotherm and PSD (the inset in (b)) of the MnO_x@C particles.

XPS were carried out to characterize the chemical state of Mn and O in hydrangea-like MnO_x@C nanocomposites. Typical XPS peaks of Mn 2p, O 1s, C 1s and Ni 2p can be observed in Fig. 4a. Specifically, the peak located at 284.6 eV (Fig. 4b) is asigned to C 1s. After pyrolysis, there are plenty of oxygen-containing functionalities remaining in the nanocomposites. This is further confirmed by the XPS analysis of O 1s (Fig. 4c), in which the peaks at 530.1, 531.6, and 533.7 eV are ascribed to Mn−O, C−O, and C=O, respectively. These oxygenated groups are beneficial for intimate anchoring MnO_x@C and enhancing the structural stability of the electrodes. The peaks at 653.5 and 641.7 eV correspond to

Mn $2p_{1/2}$ and Mn $2p_{3/2}$, respectively[41] and Mn 2p can be deconvoluted into two components (Fig. 4d), suggesting the presence of both Mn^{2+} (641.5 and 653.1 eV) and Mn^{3+} (643.4 and 654.0 eV). This is in good agreement with the result shown in EDS mapping. The mixture of Mn^{2+}/Mn^{3+} is reported to supply continuous electron transportation paths during the electrochemical process since multiple valence states can enrich the type of reaction and make the redox process smoother[42].

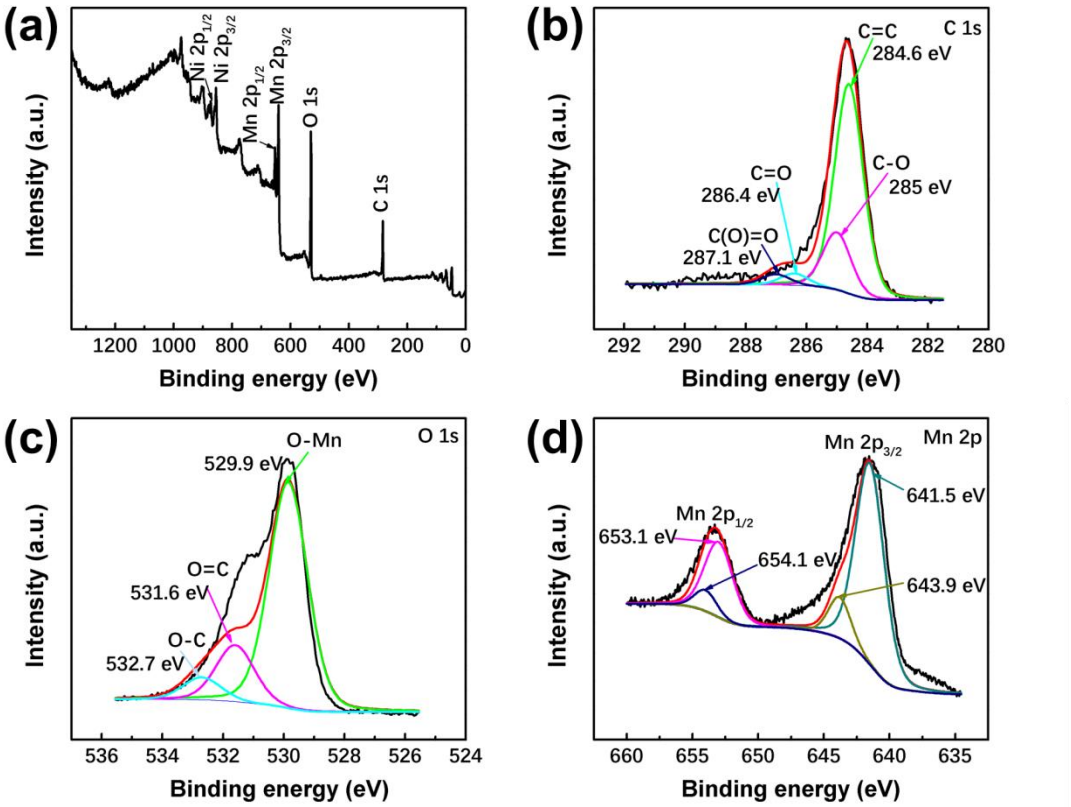

Figure 4. XPS spectra of MnO_x@C: (a) survey spectrum, (b) C 1s, (c) O 1s, (d) Mn 2p.

The electrochemical performances of MnO_x@C were systematically investigated by running cyclic voltammograms (CVs) and galvanostatic charge–discharge (GCD). Fig. 5a shows the CV curves obtaiend at different scan rates ranging from 5 to 100 mV s^{-1} within the potential window between 0.0 and 1.0 V. The shape of CV curve at low scan rate is almost rectangular as expected for a pseudocapacitance characteristic, yet it deviates accordinlgy as the scan rate increases. The GCD behaviors of the samples udner different current densities (3~12 mA cm^{-2}) in the potential window of 0.0~1.0 V were measured for the evaluation of specific capacitance. As shown in Fig. 5b, all GCD curves show a triangular shape, indicating that the electrode has good capacitive behavior. A high areal specific capacitance of 1518 mF cm^{-2} can be reached at a current density of 3 mA cm^{-2}. This performance is much superior to the electrodes based on MnO_x@Ni@C (1 mA cm^{-2}, 906.6 mF cm^{-2})[43], and 3D-porous Ni/MnO_x (0.5 mA cm^{-2}, 654 mF cm^{-2})[44]. As shown in Fig. 5c, it can be found that the areal specific capacitances are 1518, 1480, 1176, 1071, and 988.8 mF cm^{-2}, at current densities of 3, 5, 7, 9 and 12 mA cm^{-2}, respectively. To further evaluate the ion-diffusion of the electrodes, electrochemical impedance spectroscopy (EIS) were conducted. Impedance spectrum in Fig. 5d shows that the intersection with the X-axis is relatively small, indicating a small series resistance of 3.1 Ω due to the intimate contacte

between hydrangea-like MnO_x@C nanocomposites and NF without the addition of nonconductive binder which much lower than MnO_x/C (4.6 Ω) and MnO_x (6.4 Ω) synthesized via microemulsion method by PreetyAhuja and his co-workers[45, 46]. We can see that comparing with other manganese oxide materials in Table 2, our material has a higher specific capacitance at a high working voltage, mainly because the porosity of the material increases the specific surface area, leading to the energy density also increases accordingly. Due to the compounding of carbon material, the conductivity of the MnO_x is increased, and the internal resistance is mush smaller than other materials. The slope at low frequency region represents the ion diffusion resistance, which means the resistance that electrolyte diffusion in the nanocomposites. The pore size and specific surface area, which also reduced the value of the diffusion resistance.

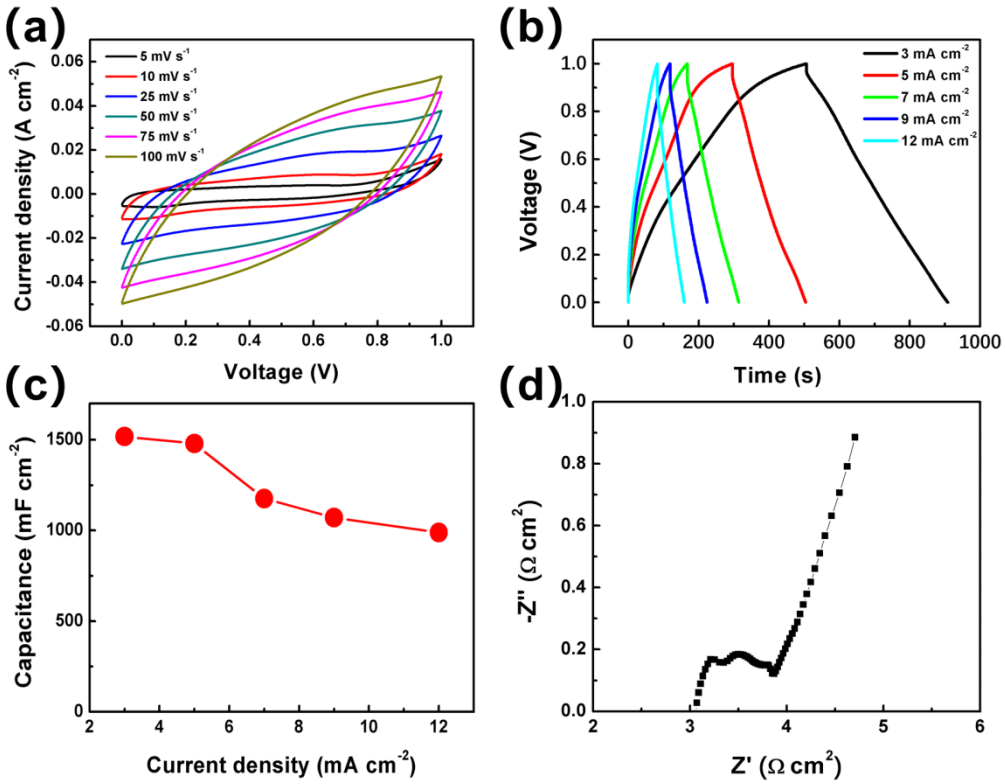

Figure 5. (a) CV curves at different scan rates, (b) Galvanostatic charge-discharge curves at different current density, (c) areal specific capacitances of MnO_x@C electrode as a function of various current densities, (d) Nyquist impedance spectra of the MnO_x@C particles.

Table 2. Comparison of the present MnO_x@C with other electrode materials based on MnO_x.

Electrode	working voltage (V)	Capacitance (F/g)	Power Density (Wkg^{-1})	Energy Density ($Wh\ kg^{-1}$)	Electrolyte	ESR value	Ref.No.
CFF/MnO_2	0-1.0	467 @$1Ag^{-1}$	175	20	Na_2SO_4 (a.q.)	4.8	[7]

MnO_2	-0.15-0.45	142 @5mAg^{-1}	-	-	KOH (a.q.)	5.5	[13]
RGO/Mn_x@ HCNs	0-1.0	210 @1.0 A g^{-1}	500	9.38	KOH (a.q.)	3.4	[25]
Mn_2O_3@NF	0-1.6	791Fg^{1} @5mVs^{-}	320	112.82	LiCl (a.q.)	3.5	[36]
-MnO_2	0-1.0	235 F g^{-1} @1mV s^{-1}	100	50	$(NH_4)_2SO_4$ (a.q.)	6.5	[40]
Mn_3O_4/γ-MnOOH	-0.2-0.8	808(1201.2 mF cm^{-2}) @3mAcm^{-2}	19.3mW cm^{-3}	1.47 mWh cm $^{-3}$	Na_2SO_4 (a.q.)	6.1	[41]
MnO_2/GCF	0-1.0	565.23 F g^{-1} @ 1 A g^{-1}	-	-	Na_2SO_4 (a.q.)	-	[42]
MnO_x@Ni@ CC	0-0.8 V	816.7(867.3 mF cm^{-2}) @1 mA cm^{-2}	0.021W cm^{-3}	1.16 mW h cm^{-3}	Na_2SO_4 (a.q.)	4.9	[43]
Ni/MnO_x	0-1.0	396.4(654 mF cm^{-2}) @0.5 mA cm^{-2}	-	-	Na_2SO_4 (a.q.)	5.0	[44]
MnO_x@C	0-1.0	1012(1518mF cm-^{2}) @3mA cm^{-2}	12.2 W cm^{-2}	169.4 mWh cm^{-2}	Na_2SO_4 (a.q.)	3.1	This work

ASC devices were assembled using MnO_x@C as cathode and activated carbon (AC) as anode in 0.5 M Na_2SO_4 gel electrolyte. The CV curves of the supercapacitor devices in Fig. 6a maintain rectangular shape when scan rate increases from 5 to 100 mV s^{-1}, suggesting a good rate performance. GCD curves of the ASC device at the current densities ranging from 5 to 12 mA cm^{-2} were also collected to further evaluate the electrochemical performance, as shown in Fig. 6b. A specific areal capacitance of 305 mF cm^{-2} is calculated from GCD curve at the current density of 5 mA cm^{-2} with 45.75% retained at 12 mA cm^{-2} (Fig. 6c). When two devices were connected in series, a red LED (10 w) can be lightened up for ~2 min after charging for 150 s (at 5 mA cm^{-2}), as shown in Fig. 6d.

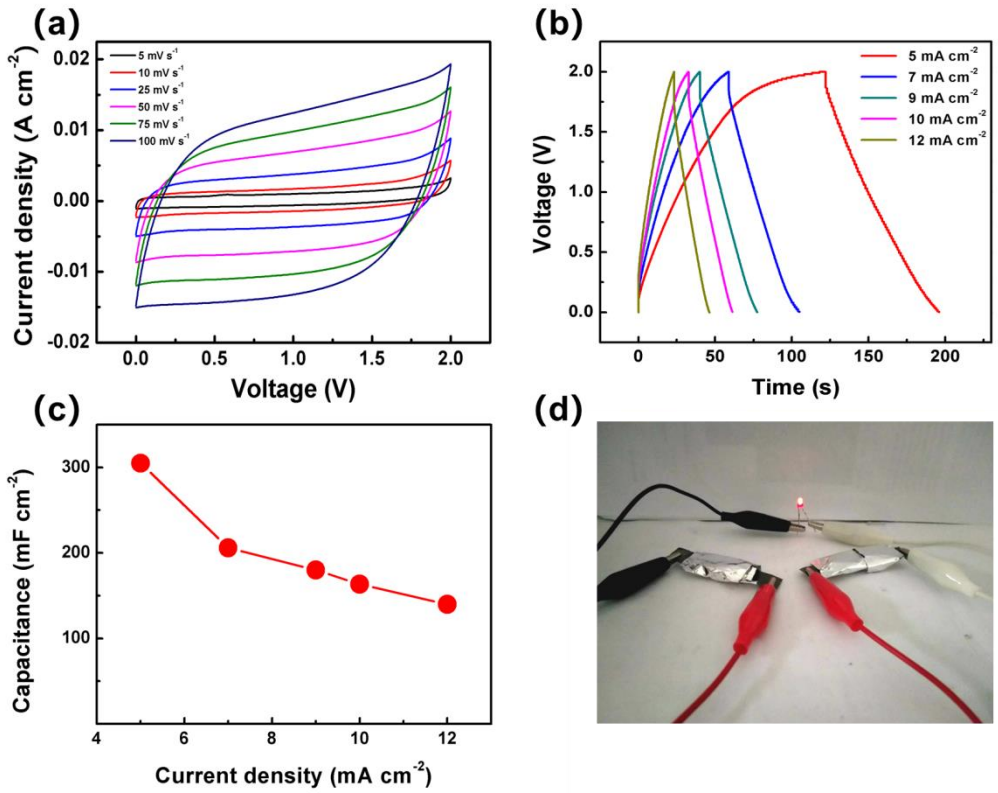

Figure 6. (a) CV curves at different scan rates, (b) GCD curves at different current densities and (c) the corresponding specific areal capacitance of ASC as a function of current densities, (d) a LED is lightened up by two ASC devices connected in series.

4. CONCLUSIONS

In summary, hydrangea-like mesoporous carbon architectures uniformly embedded with MnO_x nanoparticles (termed as MnO_x@C) were prepared. The obtained composites exhibited a high areal capacitance of 1518 mF cm^{-2} at 3 mA cm^{-2} with 65% retained at 12 mA cm^{-2}. The solid-state ASC based on MnO_x@C cathode and AC anode was fabricated, delivering a specific capacitance of 305 mF cm^{-2} at 5 mA cm^{-2} with a wide operated potential window of 2.0 V and a preferable areal energy density of 169.4 mWh cm^{-2} at the power density of 12.2 W cm^{-3}. Given the fact that MnO_x@C shows competitive electrochemical performance, the present synthesis strategy paves a new avenue of fabricating binder-free and mesoporous electrodes materials for high performance supercapacitors.

ACKNOWLEDGEMENTS
The research was financially supported from National Key Research and Development Project (2018YFE0124800), Primary Research & Development Plan of Jiangsu Province (BE2016183), Natural Science Foundation of Jiangsu Province for Youth (BK20160960), and the 14th Six Talents Peak Project of Jiangsu Province (XNYQC-016).

References

1. W. Raza, F. Ali, N. Raza, Y. Luo, K. Kim, J. Yang, S. Kumar, A. Mehmood, E.E. Kwon, *Nano Energy,* 52 (2018) 441.
2. Q. Li, Z. Li, L. Lin, X.Y. Wang, Y. Wang, C. Zhang, H. Wang, *Chem. Eng. J*., 156 (2010) 500.
3. F. Béguin, V. Presser, A. Balducci, E. Frackowiak, *Adv. Mater*., 26 (2014) 2219.
4. N. Choudhary, C. Li, J. Moore, N. Nagaiah, L. Zhai, Y. Jung, J. Thomas, *Adv. Mater*., 29 (2017) 1605336.
5. N. Wang, P. Zhao, K. Liang, M. Yao, Y. Yang, W. Hu, *Chem. Eng. J*., 307 (2017) 105.
6. M. Li, M. Zu, J. Yu, H. Cheng, Q. Li, *Small,* 13 (2017) 1602994.
7. M. Cakici, R. Kakarla, M. Alonso, *Chem. Eng. J.,* 309 (2017) 151.
8. P. Shi, L. Li, L. Hua, Q. Qian, P. Wang, J. Zhou, G. Sun, W. Huang, *ACS Nano*, 11 (2017) 444.
9. Y. Lee, K. Chang, C. Hu, Y. Chu, *J. Power Sources*, 206 (2012) 469.
10. Z. Yu, B. Duong, D. Abbitt, J. Thomas, *Adv. Mater*., 25 (2013) 3302.
11. P. Wang, Y.T. Xiao, Z.H. Zhou, J. Pu, W.J. Cao, Z. Gong, J. Hu, *Int. J. Electrochem. Sci*., 14 (2019) 287.
12. S. Zhou, H. Gao, C. Zhang, J. Yang, S. Tang, Q. Xu, S. Dong, *J. Power Sources*, 359 (2017) 585.
13. M. Xu, D. Zhao, S. Bao, H. Li, *J. Solid State Electrochem*., 11 (2007) 1101.
14. C. Park, J. Hwang, Y. Hwang, C. Song, S. Ahn, H. Kim, H. Ahn, *Electrochim. Acta*, 246 (2017) 757.
15. Adel A. Ismail1, Atif Mossad Ali, Farid A. Harraz1, Faisal, H. Shoukry, A.E. Al-Salami,*Int. J. Electrochem. Sci.*, 14 (2019) 15.
16. E. Samuel, B. Joshi, H.S. Jo, Y. Kim, S. An, M.T. Swihart, J.M. Yun, K.H. Kim, S.S. Yoon, *Chem. Eng. J*., 328 (2017) 776.
17. Y. Li, J. Xu, T. Feng, Q. Yao, J. Xie, H. Xia, *Adv. Funct. Mater*., 27 (2017) 1606728.
18. Z. Gao, H. Zhang, G. Cao, M. Han, Y. Yang, *Electrochim. Acta*, 87 (2013) 375.
19. B. Yuan, C. Xu, L. Liu, Q. Zhang, S. Ji, L. Pi, D. Zhang, Q. Huo, *Electrochim. Acta*, 104 (2013) 78.
20. J. Zhu, J. Jiang, Z. Sun, J. Luo, Z. Fan, X. Huang, H. Zhang, T. Yu, *Small*, 10 (2014) 2937.
21. J. Lin, H. Jia, H. Liang, S. Chen, Y. Cai, J. Qi, C. Qu, J. Cao, W. Fei, J. Feng, *Adv. Sci.,* 5 (2018) 1700687.
22. E. Lee, T. Lee, B. Kim, *J. Power Sources*, 255 (2014) 335.
23. D. Sun, Y. Tang, D. Ye, J. Yan, H. Zhou, H. Wang, *ACS Appl. Mater. Interfaces*, 9 (2017) 5254.
24. J. Guo, Q. Liu, C. Wang, M.R. Zachariah, *Adv. Funct. Mater*., 22 (2012) 803.
25. M. Liu, M. Shi, W. Lu, D. Zhu, L. Li, L. Gan, *Chem. Eng. J*., 313 (2017) 518.
26. Y. Xiao, Y. Cao, Y. Gong, A. Zhang, J. Zhao, S. Fang, D. Jia, F. Li, *J. Power Sources*, 246 (2014) 926.
27. S. Li, L. Yu, Y. Shi, J. Fan, R. Li, G. Fan, W. Xu, J. Zhao, *ACS Appl. Mater. Interfaces*, 11 (2019) 10178.
28. S. Zheng, X. Li, B. Yan, Q. Hu, Y. Xu, X. Xiao, H. Xue, H. Pang, *Adv. Energy Mater*., 7 (2017) 1602733.
29. T. Ladrak, S. Smulders, O. Roubeau, S.J. Teat, P. Gamez, J. Reedijk, *Eur. J. Inorg. Chem*., 2010 (2010) 3804-3812.
30. Y. Zhou, Z. Mao, W. Wang, Z. Yang, X. Liu, *ACS Appl. Mater. Interfaces*, 8 (2016) 28904.
31. A. González, E. Goikolea, J.A. Barrena, R. Mysyk, *Renewable Sustainable Energy Rev*., 58 (2016) 1189-1206.
32. C. Zhong, Y. Deng, W. Hu, J. Qiao, L. Zhang, J. Zhang, *Chem. Soc. Rev*., 44 (2015) 7484.
33. J. Yang, Z. Ma, W. Gao, M. Wei, *Chem. – Eur. J.*, 23 (2017) 631.
34. J.M. Zamaro, N.C. Pérez, E.E. Miró, C. Casado, B. Seoane, C. Téllez, J. Coronas, *Chem. Eng. J*., 195-196 (2012) 180.
35. P. Sun, R. Wang, Q. Wang, H. Wang, X. Wang, *Appl. Surf. Sci*., 475 (2019) 793.

36. M.S. Javed, H.U. Shah, N. Shaheen, R. Lin, M. Qiu, J. Xie, J. Li, R. Raza, W. Mai, C. Hu, *Electrochim. Acta,* 282 (2018) 1.
37. H. Xia, M.O. Lai, L. Lu, *J. Power Sources*, 196 (2011) 2398.
38. Z. Zeng, Y. Liu, W. Zhang, H. Chevva, J. Wei, *J. Power Sources*, 358 (2017) 22.
39. Y. Chu, L. Guo, B. Xi, Z. Feng, F. Wu, Y. Lin, J. Liu, D. Sun, J. Feng, Y. Qian, S. Xiong, *Adv. Mater.*, 30 (2018) 1704244.
40. A.J. Roberts, R.C.T. Slade, *Electrochim. Acta*, 55 (2010) 7460.
41. S.J. Meng, Z.L. Mo, Z.L. Li, R.B. Guo, N.J. Liu, *J. Solid State Chem., 3*(2019)30.
42. Z. Zhang, Y. Xiao, Y. Zhang, W. Zhang, *J Nanosci Nanotechnol*, 19(2019)9.
43. Z. Pan, Y. Qiu, J. Yang, F. Ye, Y. Xu, X. Zhang, M. Liu, Y. Zhang, *Nano Energy*, 26 (2016) 610.
44. H. Ashassi Sorkhabi, P. Lale Badakhshan, *Appl. Surf. Sci*., 419 (2017) 165.
45. Preety Ahuja, Sanjeev Kumar Ujjain, Rajni Kanojia, *Appl. Surf. Sci.*, 404 (2017) 197.
46. G. Luo, H. Huang, C. Lei, Z. Cheng, X. Wu, S. Tang, Y. Du, *Appl. Surf. Sci*., 366 (2016) 46.